3D robust anisotropic diffusion filtering algorithm for sparse view neutron computed tomography 3D image reconstruction

Yang Liu[1,2] · Teng-Fei Zhu[1] · Zhi Luo[1] · Xiao-Ping Ouyang[1,3]

Abstract

The most critical part of a neutron computed tomography (NCT) system is the image processing algorithm, which directly affects the quality and speed of the reconstructed images. Various types of noise in the system can degrade the quality of the reconstructed images. Therefore, to improve the quality of the reconstructed images of NCT systems, efficient image processing algorithms must be used. The anisotropic diffusion filtering (ADF) algorithm can not only effectively suppress the noise in the projection data, but also preserve the image edge structure information by reducing the diffusion at the image edges. Therefore, we propose the application of the ADF algorithm for NCT image reconstruction. To compare the performance of different algorithms in NCT systems, we reconstructed images using the ordered subset simultaneous algebraic reconstruction technique (OS-SART) algorithm with different regular terms as image processing algorithms. In the iterative reconstruction, we selected two image processing algorithms, the Total Variation and split Bregman solved total variation algorithms, for comparison with the performance of the ADF algorithm. Additionally, the filtered back-projection algorithm was used for comparison with an iterative algorithm. By reconstructing the projection data of the numerical and clock models, we compared and analyzed the effects of each algorithm applied in the NCT system. Based on the reconstruction results, OS-SART-ADF outperformed the other algorithms in terms of denoising, preserving the edge structure, and suppressing artifacts. For example, when the 3D Shepp–Logan was reconstructed at 25 views, the root mean square error of OS-SART-ADF was the smallest among the four iterative algorithms, at only 0.0292. The universal quality index, mean structural similarity, and correlation coefficient of the reconstructed image were the largest among all algorithms, with values of 0.9877, 0.9878, and 0.9887, respectively.

Keywords NCT · OS-SART · Sparse-view · Anisotropic diffusion filtering

Extended author information available on the last page of the article

1 Introduction

Neutron computed tomography (NCT) is a nondestructive testing technique that can accurately and rapidly detect the internal structure of a samples [1–3]. NCT has been extensively used in a variety of domains, including porous media, biology, special nuclear materials, and archaeology [4–10], because of its strong neutron penetration into thick metals. Equipment for X-ray and neutron imaging has substantially improved with the rapid advancement in electronic information technology. Advanced imaging instruments and high-quality image processing algorithms continue to be explored and applied to 3D tomography and sample visualization, such as the large-area 3He tube array detector used for China spallation neutrons [11]. Owing to the strong penetration of neutrons, in some special cases, they can be used as a

complement to X-ray CT to provide better imaging results. NCT begins by rotating a test object to obtain neutron projection images at different angles, followed by processing the projection images using reconstruction algorithms to obtain 2D or 3D tomographic images [12, 13]. Additionally, machine learning is an emerging research tool that has seen a gradual increase in its use in radiation imaging and image processing, and has led to many innovations and advances in nuclear energy science and nuclear technology [14].

Neutron sources produce neutron beams, and are commonly used in fields such as materials research, neutron photography, and nuclear physics. Neutron sources can be divided into accelerator- and reactor-driven neutron sources. Several nations and international organizations are working to promote the construction and development of neutron source facilities such as accelerator-driven compact neutron sources, owing to the significance of neutron photography and neutron sources in scientific research and engineering applications [15–19]. Neutron source types range from radioactive to large neutron sources. The neutron sources used in NCT systems are generally of low intensity, with neutron fluxes ranging from 105 to 10^{10} n/cm^2 [20]. Because of the low neutron flux, the time required for a single projection scan is relatively long, which leads to low-quality neutron projection data. Therefore, improving the quality of neutron imaging is a major research topic in NCT. There are two general approaches for improving the quality of neutron tomography imaging. The first is to shorten the time required for a single scan by increasing the strength of the neutron source, which is difficult to achieve. The second method enhances the quality of NCT-recovered images by employing effective image-reconstruction algorithms. The primary algorithms used in NCT systems are analytical and iterative. The analysis algorithm requires complete projection data to reconstruct a high-quality image; therefore, it cannot be applied to sparse reconstruction. Since iterative reconstruction can embed a priori information, it is promising for applications in sparse reconstruction. The iterative algorithms include ART [21], SIRT [22], and SART [23]. The development of the compressive sensing theory has led to the successful application of total variance (TV)-based algebraic iterative reconstruction algorithms for CT reconstruction. To reduce noise and effectively preserve edge and structure detail information, Rudin proposed a denoising model using the total variance as a rule constraint, which has excellent results in preserving edges [24]. Several studies have proposed including directional TV [25], anisotropic TV [26], edge-preserving TV [27], and weighted TV [28].

The TV-based denoising algorithm performs the same function for different regions of an image. Although this method can effectively remove noise, it inevitably considers a part of the image detail information as the object of the noise reduction process, which is an important feature that we focus on when processing images. Therefore, it is important to protect detailed image information during image denoising. In recent years, through an in-depth study of the governing partial differential equations (PDEs), it has been found that the anisotropic diffusion model can solve this problem to a certain extent, and its adaptive smoothing function can be smoothed to different degrees according to different image features to preserve the edge details based on retaining image noise reduction information. The PDE-based anisotropic diffusion model can reduce noise by enhancing diffusion in the flat regions of the image, and can also be utilized to reduce diffusion at the edges of the image to preserve edge detail information. This is due to the fact that the PDE-based image processing method smooths only the parallel edges of the projection data and not the vertical edges, thus preserving the main features of the image while reducing noise and smoothing the image. The projection data obtained in the NCT system exhibited a high level of noise, which had a direct impact on the quality of the reconstructed image. Recently, several studies have been conducted on the use of anisotropic diffusion filters for image manipulation. In 1990, Perona and Malik first used the gradient as an edge detector to derive each anisotropic diffusion model, merging diffusion sparsity into the filtering process such that it diffused in the smooth region and stopped diffusing in the edge region [29]. You and Kaveh [30] proposed a fourth-order partial differential model using the Laplace algorithm to describe the image smoothing map, which eliminates the "step effect" of the second-order partial differential model, but the noise reduction efficiency required further improvement. Baxi and Feng [31] proposed a fractional-order variational model to improve noise reduction efficiency. Alvarez et al. [32] introduced a mean curvature equation of motion for anisotropic diffusion that considers the directional information of the edges and varies only in the direction of the minimum gradient, and not in the direction of the maximum gradient during the diffusion process. Thus, the image is smoothed only in an orientation parallel to the edge. Although there are many anisotropic diffusion noise reduction methods, all of them have diffusion strengths that use gradient information to effectively detect edges. Therefore, when the edge is heavily contaminated by noise, these methods may not be able to detect the edges and preserve the other features protected by that edge. This requires a more sophisticated diffusion-based noise-reduction model than edge detection.

Therefore, in this study, we propose an efficient 3D reconstruction algorithm for NCT that extends the 2D anisotropic diffusion filter to 3D applications of NCT imaging. Our primary goal is to eliminate noise and artifacts that appear in sparse-view projection reconstruction. To achieve this goal, we propose the ordered subset simultaneous algebraic

reconstruction technique (OS-SART) anisotropic diffusion filtering (ADF) algorithm based on the analysis of traditional image filtering algorithms, which uses the OS-SART algorithm for image reconstruction and applies an anisotropic diffusion filter to remove image noise in the reconstruction process while preserving the structural information of the image edges.

2 Algorithms

2.1 TV algorithm

Rudin, Osher, and Fetamin proposed an ROF model using the L1 parameterization of the image gradient as regularization [24]. The model uses TV regularization to minimize the total variance and improve the image quality. The ROF model uses the L1 norm in the minimization process, which maintains the nonlinear characteristics of the image and thus allows more image edge structures to be retained. The expression for this model is as follows:

$$f_{\text{reg}} = \arg\min \left\{ \|p - wf\|_2^2 + \lambda \|f\|_{\text{TV}} \right\}, \tag{1}$$

where $\|p - wf\|_2^2$ is a data fidelity item and $\|f\|_{\text{TV}}$ is the regularization term, which is the TV norm of the image. The TV norm is the L1 norm of the image gradient, and can be expressed as follows:

$$\|f\|_{\text{TV}} = \sum \sqrt{|\nabla_x f|^2 + |\nabla_y f|^2 + |\nabla_z f|^2}, \tag{2}$$

where f denotes a 3D image, ∇f_i represents the gradient along the i direction, and $|\cdot|$ represents the complex modulus.

2.2 Split Bregman solved total variation (SBTV)

The Bregman distance [33], also known as the Bregman scatter, between two points u and v, is defined by the following equation:

$$D_E^p(u, v) = E(u) - E(v) - \langle p, u - v \rangle, \tag{3}$$

where $E(u)$ is a convex function, p denotes the subgradient of $E(u)$, and $\langle , \rangle$ denote the inner product.

In the optimization problem, the Bregman distance is introduced as a regularization term. The Bregman iterative regularization method can be expressed using the imaging principle formula as follows:

$$u^{k+1} = \min_u D_E^{p^k}(u, u^k) + \frac{u}{2}\|Au - f\|_2^2, \tag{4}$$

since Eq. (4) is a convex optimization problem. Substituting this into Eq. (5), the following results can be obtained using the optimal conditions:

$$p^{k+1} = p^k - \mu A^{\text{T}}(Au^{k+1} - f). \tag{5}$$

The Bregman iterative method comprises Eqs. (4) and (5). Equation (4) optimizes the subproblem, and Eq. (5) updates the search direction of the iterative solution. However, owing to the difficulty of the subgradient calculation, the two equations above are only warped according to the nature of recursion. Therefore, Bregman's iterative method is obtained in a simplified form [34] as

$$\begin{aligned} u^{k+1} &= \min_u E(u) + \frac{u}{2}\|Au - f - b\|_2^2 \\ b^{k+1} &= b^k + (Au^{k+1} - f). \end{aligned} \tag{6}$$

When used to reconstruct NCT images, the reconstruction algorithm did not provide satisfactory reconstruction results. Therefore, the image must be preprocessed, and generally good results are achieved using the denoising TV method. The objective function of image denoising using the split-Bregman method is expressed as follows:

$$\min_f |\nabla_x f| + |\nabla_y f| + |\nabla_z f| + \frac{\mu}{2}\|f - f^{it}\|_2^2. \tag{7}$$

Solving Eq. (7) using the split Bregman method transforms the problem into three easily solvable subproblems. Therefore, transforming Eq. (7) into a constrained problem, it can be expressed as:

$$\min_{f, d_x, d_y, d_z} |d_x| + |d_y| + |d_z| + \frac{\mu}{2}\|f - f^{it}\|_2^2, \tag{8}$$

where $d_x = \nabla_x f, d_y = \nabla_y f, d_z = \nabla_z f$ Subsequently, using Bregman iteration, we solved Eq. (7), which can be further expressed as

$$\begin{aligned} \min_{f, d_x, d_y, d_z} &|d_x| + |d_y| + |d_z| + \frac{\mu}{2}\|f - f^{it}\|_2^2 + \frac{\lambda}{2}\|d_x^k - \nabla_x d - b_x^k\|_2^2 \\ &+ \frac{\lambda}{2}\|d_y^k - \nabla_y d - b_y^k\|_2^2 + \frac{\lambda}{2}\|d_z^k - \nabla_z d - b_z^k\|_2^2 \\ f^{k+1} = \min_f &\frac{\mu}{2}\|f - f^{it}\|_2^2 + \frac{\lambda}{2}\|d_x^k - \nabla_x f - b_x^k\|_2^2 \\ &+ \frac{\lambda}{2}\|d_y^k - \nabla_y f - b_y^k\|_2^2 + \frac{\lambda}{2}\|d_z^k - \nabla_z f - b_z^k\|_2^2 \\ d_i^{k+1} = \min_{d_i} &\|d_i\|_1 + \|d_i - \nabla_i f^{k+1} - b_i^k\|_2^2. \end{aligned} \tag{9}$$

As we have observed, the split Bregman approach differentiates the problem by separating the L1 part. We applied the Gauss–Seidel method [35] to solve f in a simpler manner, as follows:

$$
\begin{aligned}
f_{g,j,v}^k = \frac{\lambda}{\mu + 6\lambda}(&f_{g+1,j,v}^k + f_{g-1,j,v}^k + f_{g,j+1,v}^k \\
&+ f_{g,j-1,v}^k + f_{g,j,v+1}^k + f_{g,j,v-1}^k \\
&+ d_{x,g-1,j,v}^k - d_{x,g,j,v}^k + d_{y,g,j-1,v}^k \\
&- d_{y,g,j,v}^k + d_{z,g,j,v-1}^k - d_{z,g,j,v}^k \\
&- b_{x,g-1,j,v}^k + b_{x,g,j,v}^k - b_{y,g,j-1,v}^k + b_{y,g,j,v}^k \\
&- b_{z,g,j,v-1}^k + b_{z,g,j,v}^k) + \frac{\lambda}{\mu + 6\lambda}f_{g,j,v}.
\end{aligned}
\tag{10}
$$

Additionally, since the parts of d are unrelated, they can be separated into d_x, d_y, and d_z. Thus, we employ the shrinkage operator to obtain the optimal solution [36], which can be written as follows:

$$
d_i^{k+1} = shink\left(\nabla_i f^{k+1} + b_i^k, \frac{1}{\lambda}\right) = \frac{\nabla_i f^{k+1} + b_i^k}{\left|\nabla_i f^{k+1} + b_i^k\right|} \times \max\left(\left|\nabla_i f^{k+1} + b_i^k\right| - \frac{1}{\lambda}, 0\right).
\tag{11}
$$

2.3 3D anisotropic diffusion filtering algorithms (3D-ADF)

Sun et al. extended two-dimensional anisotropic diffusion filtering to three dimensions and proposed a three-dimensional anisotropic diffusion filtering algorithm that can retain image edge structure information, as well as perform denoising [37]. Drawing on this algorithm, we introduced it into CT reconstruction.

$$
\frac{\partial f(i, l, r; t)}{\partial t} = div[q(i, l, r; t)\nabla f(i, l, r; t)],
\tag{12}
$$

where f denotes the three-dimensional image, ∇ represents the gradient operator, and div denotes the diffusion coefficient. Current research on anisotropic diffusion-filtering algorithms focuses on the selection of $q(x)$. For, example, the $q(x)$ is expressed as follows:

$$
q(i, l, r; t) = \frac{1}{1 + \left[\frac{|\nabla f(i,l,r;t)|^2}{f(i,l,r;t)^2} - p^2\right]/(p^2(1+p^2))}.
\tag{13}
$$

The equation for the diffusion coefficient of 3D anisotropic diffusion is

$$
q(h) = \frac{1}{1 + \left[h^2(i, l, r; t) - h_0^2(t)\right]/\left[h_0^2(t)(1 + h_0^2(t))\right]}
\tag{14}
$$

$$
h_0(t) = \frac{\sqrt{\mathrm{var}[z(t)]}}{\overline{z(t)}},
\tag{15}
$$

where $\mathrm{var}[z(t)]$ denotes the intensity variance, and $\overline{z(t)}$ represents the average value of the artifacts area at position t.

The expression for the instantaneous coefficient of variation $h(i, l, r; t)$ in three dimensions is as follows:

$$
h(i, l, r; t) = \sqrt{\frac{(1/3)(|\nabla f|/f)^2 - (1/6)^2(\nabla^2 f/f)^2}{(1 + (1/6)(\nabla^2 f/f))^2}}.
\tag{16}
$$

These algorithms not only remove noise, but also retain more information about the image edge structure.

$$
\begin{aligned}
\frac{\partial f(i, l, r; t)}{\partial t} &= div[q(i, l, r; t)\nabla f(i, l, r; t)] \\
f(i, l, r; 0) &= f_0(i, l, r).
\end{aligned}
\tag{17}
$$

In order to solve Eq. (17), it was discretized, and the discrete expression of the 3D anisotropic diffusion is obtained as in Eq. (18):

$$
f_{g,j,k}^k = f(gh, jh, vh, k\Delta t)
$$

$$
\begin{cases}
f_{g,j,v}^{k+1} = f_{g,j,v}^k + \dfrac{\Delta t}{6}d_{g,j,v}^k \\[2mm]
d_{g,j,v}^k = \dfrac{1}{h^2}\left[\begin{array}{l} q_{g+1,j,v}^k(f_{g+1,j,v}^k - f_{g,j,v}^k) + q_{g,j,v}^k(f_{g-1,j,v}^k - f_{g,j,v}^k) \\ + q_{g,j+1,v}^k(f_{g,j+1,v}^k - f_{g,j,v}^k) \end{array}\right]. \\[3mm]
+ \dfrac{1}{h^2}\left[\begin{array}{l} q_{g,j,v}^k(f_{g-1,j,v}^k - f_{g,j,v}^k) + q_{g,j,v+1}^k(f_{g,j,v+1}^k - f_{g,j,v}^k) \\ + q_{g,j,v}^k(f_{g,j,v-1}^k - f_{g,j,v}^k) \end{array}\right]
\end{cases}
\tag{18}
$$

2.4 OS-SART algorithm

The OS-SART algorithm is a variant of the SART algorithm. By repeatedly breaking up the projection data into ordered subgroups for each subset, the computing efficiency of SART is increased. At each iteration, the algorithm reconstructs a subset of the image based on the corresponding projected subset. This procedure was repeated for each subgroup, and the results were combined to create a final reconstructed image. By using ordered subsets, OS-SART creates a tradeoff between the computation time and image quality. It provides faster reconstruction speeds than conventional SART, while still achieving better image quality. By varying the number of subsets and iterations, the equilibrium between the reconstruction speed and image accuracy can be regulated. The formula is given by the equation below:

$$f_j^{(k+1)} = f_j^k + \frac{\sum_{i \in S_i} \left\{ \lambda_k \frac{p_i - \sum_{m=0}^{M-1} w_{im} f_{im}^{(k)} w_{ij}}{\sum_{m=0}^{M-1} w_{im}} \right\}}{\sum_{i \in S_i} w_{ij}}, \quad (19)$$

where i represents the i-th ray at a particular projection angle, j refers to the pixel value in the i-th ray, k represents the number of iterations, and λ is a relaxation factor.

2.5 Proposed algorithm

Based on the OS-SART image reconstruction and 3D ADF image processing algorithms, we presented a sparse reconstruction algorithm (OS-SART-ADF) for NCT. The algorithm comprises two loops: the outer loop employs OS-SART for image reconstruction, and the inner loop employs ADF for image denoising.

3 Experimental

3.1 Quantitative evaluation index

The correlation coefficient (CC) is a commonly used metric in image evaluation that utilizes the covariance between the pixel values of two images to measure the correlation between them using the following formula:

Table 1 OS-SART-ADF algorithm

1. Initialization: f_0, *et1*
2. while $\|f^k - f^{k-1}\|_2^2 \geq et1$
3. Step 1: OS-SART reconstruct the image
4. for n = 1 to $N_{OS\text{-}SART}$ do
5. $f_j^{(k+1)} = f_j^k + \frac{\sum_{i \in S_i} \left\{ \lambda_k \frac{p_i - \sum_{m=0}^{M-1} w_{im} f_{im}^{(k)} w_{ij}}{\sum_{m=0}^{M-1} w_{im}} \right\}}{\sum_{i \in S_i} w_{ij}}$
6. Step 2: ADF
7. while the stop criterion is not met
8. $f_{g,j,k}^k = f(gh, jh, vh, k\Delta t)$

$$\begin{cases} f_{g,j,v}^{k+1} = f_{g,j,v}^k + \frac{\Delta t}{6} d_{g,j,v}^k \\ d_{g,j,v}^k = \frac{1}{h^2} \begin{bmatrix} c_{g+1,j,v}^k (f_{g+1,j,v}^k - f_{g,j,v}^k) + c_{g,j,v}^k (f_{g-1,j,v}^k - f_{g,j,v}^k) \\ + c_{g,j+1,v}^k (f_{g,j+1,v}^k - f_{g,j,v}^k) \end{bmatrix} \\ + \frac{1}{h^2} \begin{bmatrix} c_{g,j,v}^k (f_{g-1,j,v}^k - f_{g,j,v}^k) + c_{g,j,v+1}^k (f_{g,j,v+1}^k - f_{g,j,v}^k) \\ + c_{g,j,v}^k (f_{g,j,v-1}^k - f_{g,j,v}^k) \end{bmatrix} \end{cases}$$

9. end
10. end
11. obtain the final image

$$CC = \frac{\sum_{k=1}^{M} (\varpi(y) - \overline{\varpi})(\varpi_{true}(y) - \overline{\varpi}_{true})}{\left\{ \sum_{k=1}^{M} (\varpi(y) - \overline{\varpi})^2 \sum_{y=1}^{M} (\varpi_{true}(y) - \overline{\varpi}_{true})^2 \right\}^{1/2}}, \quad (20)$$

where $\overline{\varpi}_{true}$ represents the measurement image, M denotes the voxel number, and $\varpi(y)$ represents the reconstructed value at voxel y.

The mean structural similarity (MSSIM) was used to measure the structural similarity between two images. This takes into account information such as contrast, brightness, and structure of the image to provide a more comprehensive evaluation.

$$\text{Brightness information}: \quad l(\varepsilon, \eta) = \frac{2u_\varepsilon u_\eta + C_1}{u_\varepsilon^2 + u_\eta^2 + C_1}$$

$$\text{Contrast information}: \quad c(\varepsilon, \eta) = \frac{2\sigma_\varepsilon \sigma_\eta + C_2}{\sigma_\varepsilon^2 + \sigma_\eta^2 + C_2}$$

$$\text{Structure Information}: \quad s(\varepsilon, \eta) = \frac{\zeta_{\varepsilon\eta} + C_3}{\zeta_\varepsilon + \zeta_\eta + C_2}$$

where ε, η represents the reference image and measurement image, separately; u_ε and u_η are the averages of the image, σ_ε and σ_η are the standard deviations of the image, $\zeta_{\varepsilon\eta}$ is the covariance of the image, and C_1, C_2, and C_3 are constants. Therefore, the MSSIM formula is as follows:

$$\text{MSSIM} = \frac{1}{M} \sum_{t=1}^{M} \left[l(\varepsilon_t, \eta_t) \right]^\alpha \times \left[c(\varepsilon_t, \eta_t) \right]^\beta \times \left[s(\varepsilon_t, \eta_t) \right]^\gamma. \quad (21)$$

The root mean square error (RMSE) is used to measure the difference between two images; it is a measure of similarity between two images obtained by calculating the difference between their corresponding pixel values.

$$\text{RMSE} = \sqrt{\frac{\sum_{n=1}^{N} (\overline{f_n} - f_n)}{N}}, \quad (22)$$

Here, $\overline{f_n}$ denotes a voxel in the measurement image, f_n denotes a voxel in the sample, and N denotes the number of voxels.

The universal quality index (UQI) is an objective metric used to measure the quality of an image, and is calculated by comparing the differences in structure, brightness, and contrast between a reference image and measurement image.

$$\text{UQI} = \frac{2\text{cov}(\overline{\mu}, \mu)}{\overline{\rho}^2 + \rho^2} \cdot \frac{2\overline{\mu}\mu}{\overline{\mu}^2 + \mu^2}, \quad (23)$$

In the above equation, cov denotes the pixel value covariance of the reference and measurement images, $\overline{\mu}$ and μ denote the mean pixel values of the reference and measurement images, respectively, and $\overline{\rho}^2$ and ρ^2 represent the standard deviation of the pixel values of the reference and measurement images, respectively.

3.2 Neutron noise model

Photon statistical noise is a statistical fluctuation in the number of photons received per pixel by the detector owing to the limited number of rays. The photon statistical noise obeys a Poisson distribution and manifests itself as random variations in the image, particularly in low-dose scans. Electronic noise is generated by the detectors and electronics in the CT system and can affect the quality of the image. The electronic noise typically follows a Gaussian distribution. Additionally, a variety of noise is present in PET, MRI, and other imaging systems, and various algorithms and filters must be used in the reconstruction of images from these imaging systems to minimize the effects of noise and retain useful information [38, 39]. The following equation can be used in NCT imaging to represent the noise model of the system:

$$\overline{L} = Poisson(L) + Gaussian(m_{ic} + \delta_{ic}^2), \tag{24}$$

where $\overline{L}$ denotes noisy transmission data, L is the mean number of photons, m_{ic} and δ_{ic}^2 are the mean and variance of the noise of the electronic device, respectively. The value m_{ic} is generally set to zero when commissioning the system. The variance δ_{ic}^2 is assessed by dark current measurements [40]. In this study, three parameters, the photon incident flux 1×10^5, $m_{ic} = 0$, and $\delta_{ic}^2 = 0.25$ were set based on the characteristics of the NCT system.

3.3 Digital 3D Shepp–Logan model experiment

By reconstructing the digital 3D Shepp–Logan model with dimensions of $256 \times 256 \times 256$, we compare and assess the performance variances of four algorithms: filtered backprojection (FBP), OS-SART-TV, OS-SART-SBTV, and OS-SART-ADF, by reconstructing the digital 3D Shepp–Logan model of size $256 \times 256 \times 256$. A slice image of the 3D Shepp–Logan mode at $z = 128$ is shown in Fig. 1. The three iterative algorithm parameters are specified as follows: OS-SART-TV, $\lambda_{OS-SART} = 2.2$, $Niter_{OS-SART} = 50$, $\lambda_{TV} = 200$, and $Niter_{TV} = 300$. As for the OS-SART-SBTV algorithm, $\lambda_{OS-SART} = 2.2$, $Niter_{OS-SART} = 50$, $\lambda_{SBTV} = 0.0032$, and $Niter_{SBTV} = 150$. As for the OS-SART-ADF algorithm (Table 1), $\lambda_{OS-SART} = 2.2$, $Niter_{OS-SART} = 50$, $\lambda_{ADF} = 0.002$, and $Niter_{ADF} = 300$.

Fig. 1 3D Shepp–Logan slice image at $z = 128$

The images produced by the four algorithms for reconstructing the different projection angles are shown in Fig. 2. The findings of all the algorithms show that an increase in the projected angle count significantly improves the smoothness of the reconstructed image and sharpness of the edge structure. When comparing the iterative reconstruction results, the reconstructed image of the FBP algorithm revealed significant artifacts caused by the algorithm's design defects. By comparison, the images reconstructed using the three iterative algorithms had clearer edge-structure information. From the region of interest in Fig. 2, it is clear that although OS-SART-TV can effectively reduce artifacts, the fine structure of the image is lost more significantly, resulting in the reconstructed image being too smooth. When the number of sparse views is 25, OS-SART-SBTV can also reconstruct clearer structural information of the image, but there is still ambiguity, in contrast to OS-SART-ADF. By comparing the reconstructed images from the different algorithms, it was observed that the OS-SART-ADF algorithm effectively eliminated image noise and clearly reconstructed the edge structure of the image.

We compared and analyzed the error images reconstructed using the five algorithms. The difference in pixel values between the original and reconstructed images at the same locations is reflected in the error image; the smaller the difference, the more structural information is included in the reconstructed image. From the error images in Fig. 3, the error image of FBP has the largest difference, indicating that the algorithm reconstructs the image with a large amount of structural feature information lost. In comparison with the analytical FBP algorithm, all these iterative algorithms performed well in removing artifacts and reconstructing the
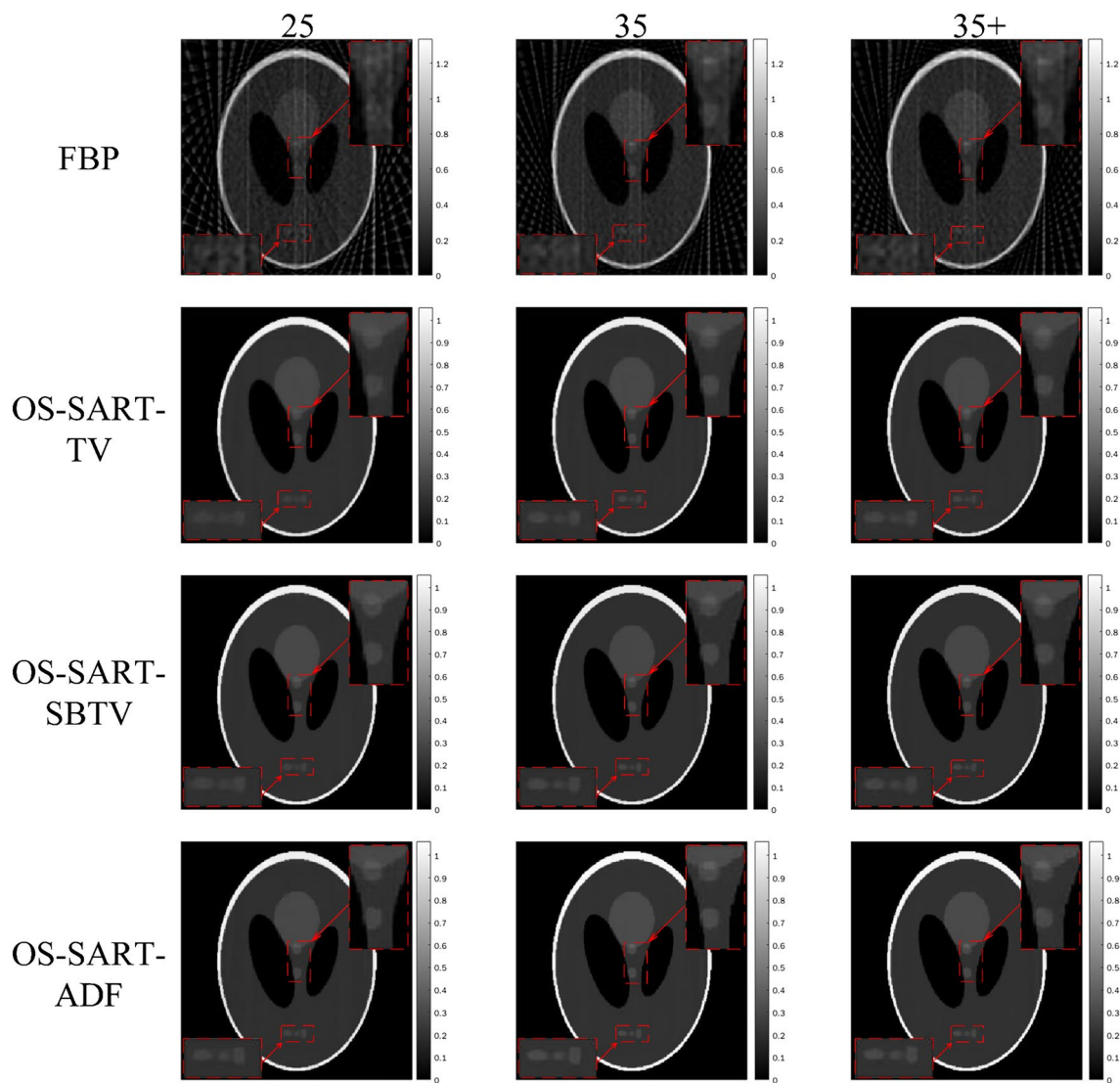
Fig. 2 Sliced reconstructed images at z = 128 for the four algorithms

detailed structural information of the image. However, OS-SART-ADF had the least error in the image pixel values, indicating that it reconstructed the most detailed image.

The reconstructed image contours of all algorithms are shown in Fig. 4 to provide an in-depth analysis of their reconstruction performance. From left to right, the projected views are 25, 35, and 35 +, where 35 + denotes the image reconstructed with the added neutron noise model. The profile lines of the FBP-rebuilt image differ significantly from those of the reconstructed image, as shown in Fig. 4. Although OS-SART-TV and OS-SART-SBTV are superior to FBP, their reconstructed image profiles deviate slightly from the profiles of the reference image. In comparison, OS-SART-ADF reconstructs images whose profiles are most similar to the reference image. These results further demonstrate that OS-SART-ADF is highly appropriate for NCT.

The image quality of each algorithm was quantitatively evaluated using four image assessment indices, as shown in Fig. 5. We first analyzed all algorithms that reconstructed the image obtained with noiseless projection data. The image evaluation indices gradually decreased with the reduction in the projection angle according to the three image evaluation metrics CC, MSSIM, and UQI; the change trends of these metrics were identical. From the RMSE metric in Fig. 5, it can be seen that the OS-SART-ADF-reconstructed images had the minimum RMSE values under the same conditions. For instance, the RMSE of the OS-SART-ADF-reconstructed image is 0.0292 when the reconstructed projection view is 25, which demonstrates that the algorithm reconstructs the image with pixel values closest to the original values, and that the reconstructed image has the best quality. From the UQI metric in Fig. 5d, it can be seen that the UQI
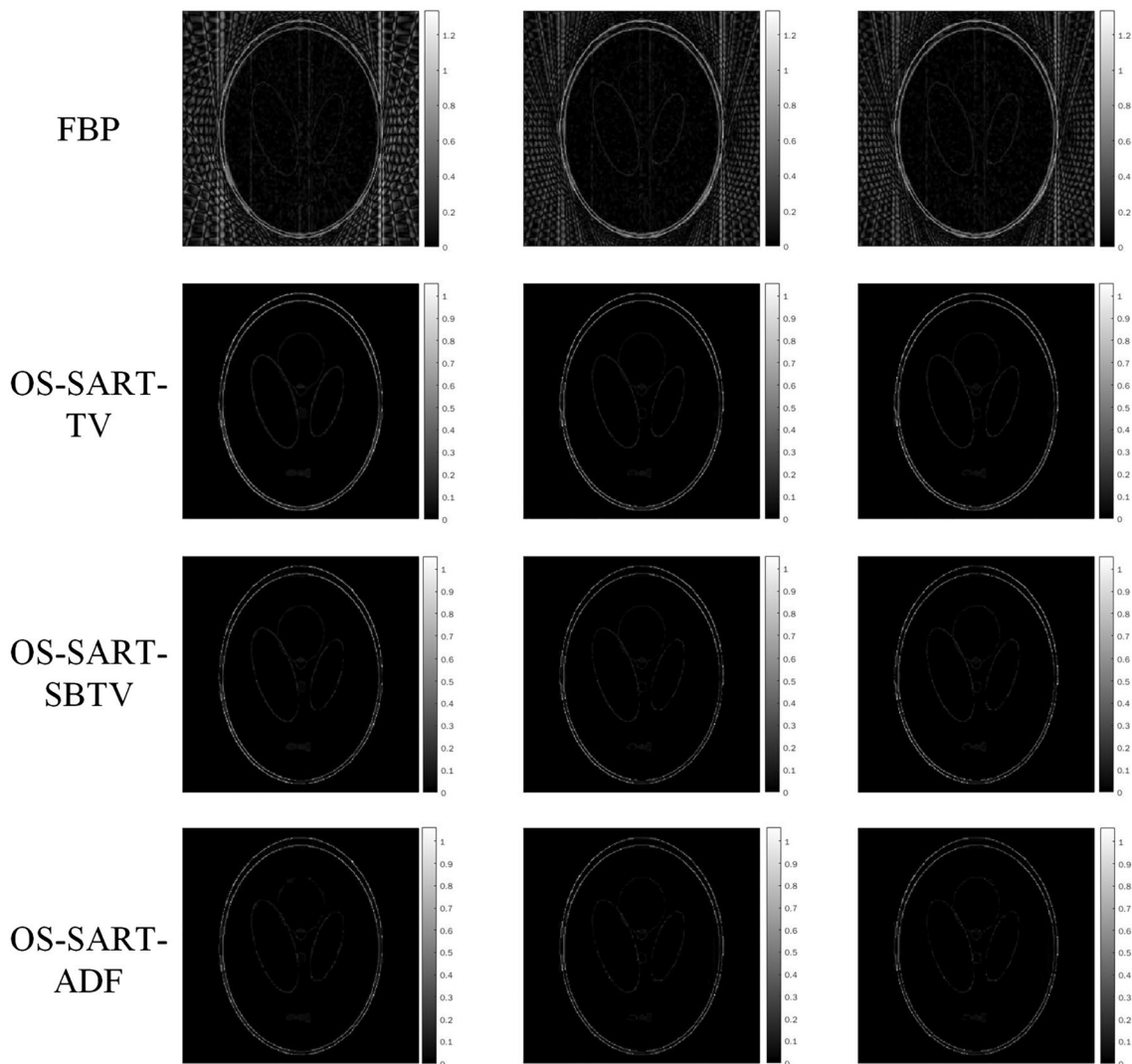
Fig. 3 The slice of the error images at $z = 128$

of all algorithms progressively increases with the number of projection views, which is opposite to the trend of the RMSE. OS-SART-ADF has the highest UQI for reconstructing images under identical conditions compared to all other reconstruction methods, indicating its superior performance. When OS-SART-ADF reconstructed the 25 projection views, the UQI, MSSIM, and CC of the reconstructed image were 0.9877, 0.9878, and 0.9887, respectively. These evaluation metrics of the OS-SART-ADF-reconstructed image were the highest among the three iterative algorithms. Subsequently, we analyzed the reconstructed images containing noisy projection data. It can be observed from the CC, MSSIM, and UQI in Fig. 5 that these metrics are maximized for the OS-SART-ADF algorithm-reconstructed images when the reconstructed projection views are the same, with values of 0.991, 0.9903, and 0.9901, respectively. The RMSE of the OS-SART-ADF-reconstructed images was minimized

according to the RMSE in Fig. 5. As a result, when the reconstructed projection angles are the same, OS-SART-ADF has the best quality of reconstructed images, based on an examination of the reconstructed images.

3.4 3D Industrial phantom

To further verify the performance of the OS-SART-ADF in real-world situations, we compared the reconstructed images of a 3D industrial model with dimensions of $256 \times 256 \times 256$. A sliced image of the 3D industrial model at $z = 128$ is shown in Fig. 6. By reconstructing the 3D industrial model, we evaluated the ability of each algorithm to retain structural information at the edges of the image.

Figure 7 shows the reconstructed images for each algorithm when reconstructing the 3D industrial model at
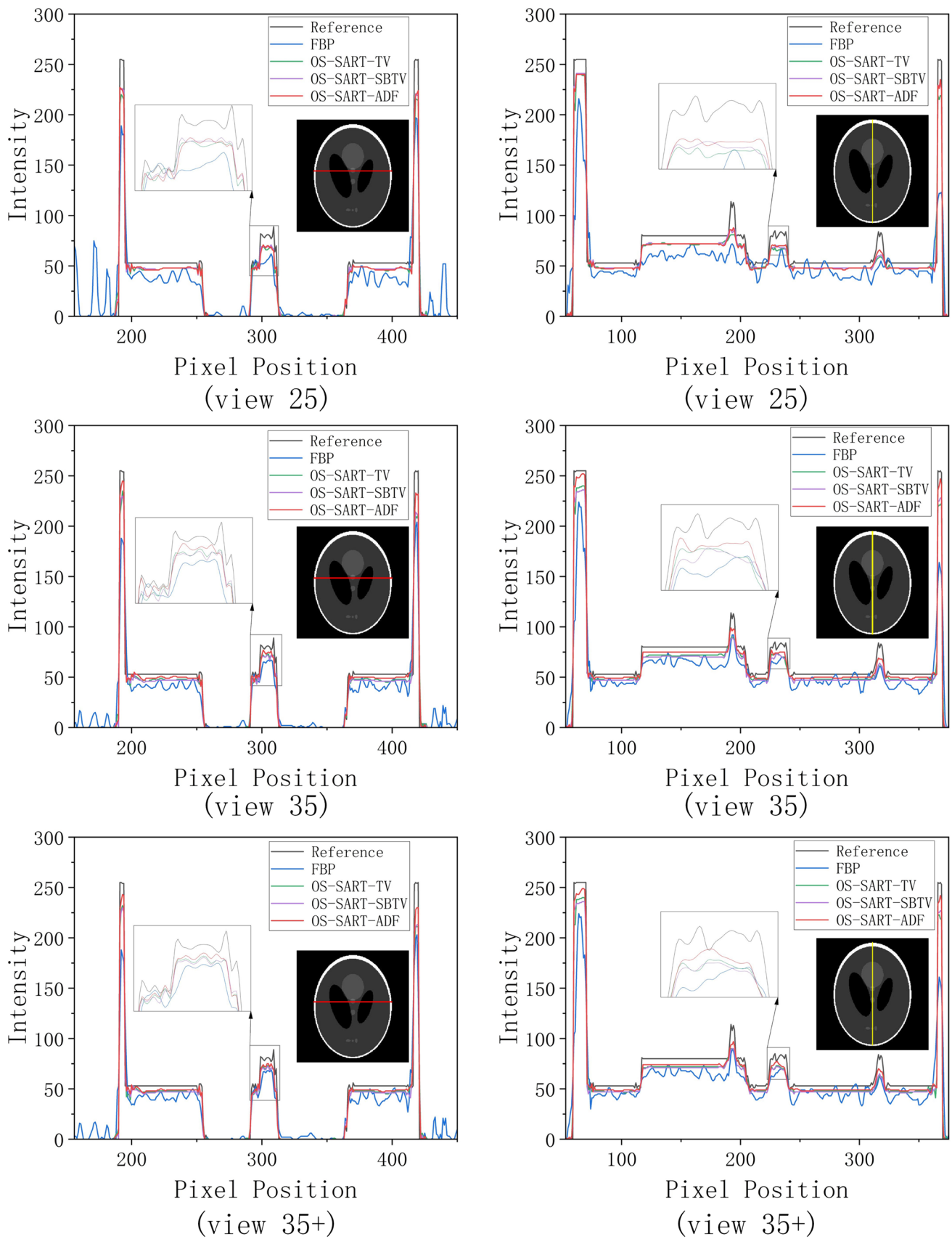
Fig. 4 Profiles of reconstructed images using different algorithms: **a** horizontal profile and **b** vertical profile
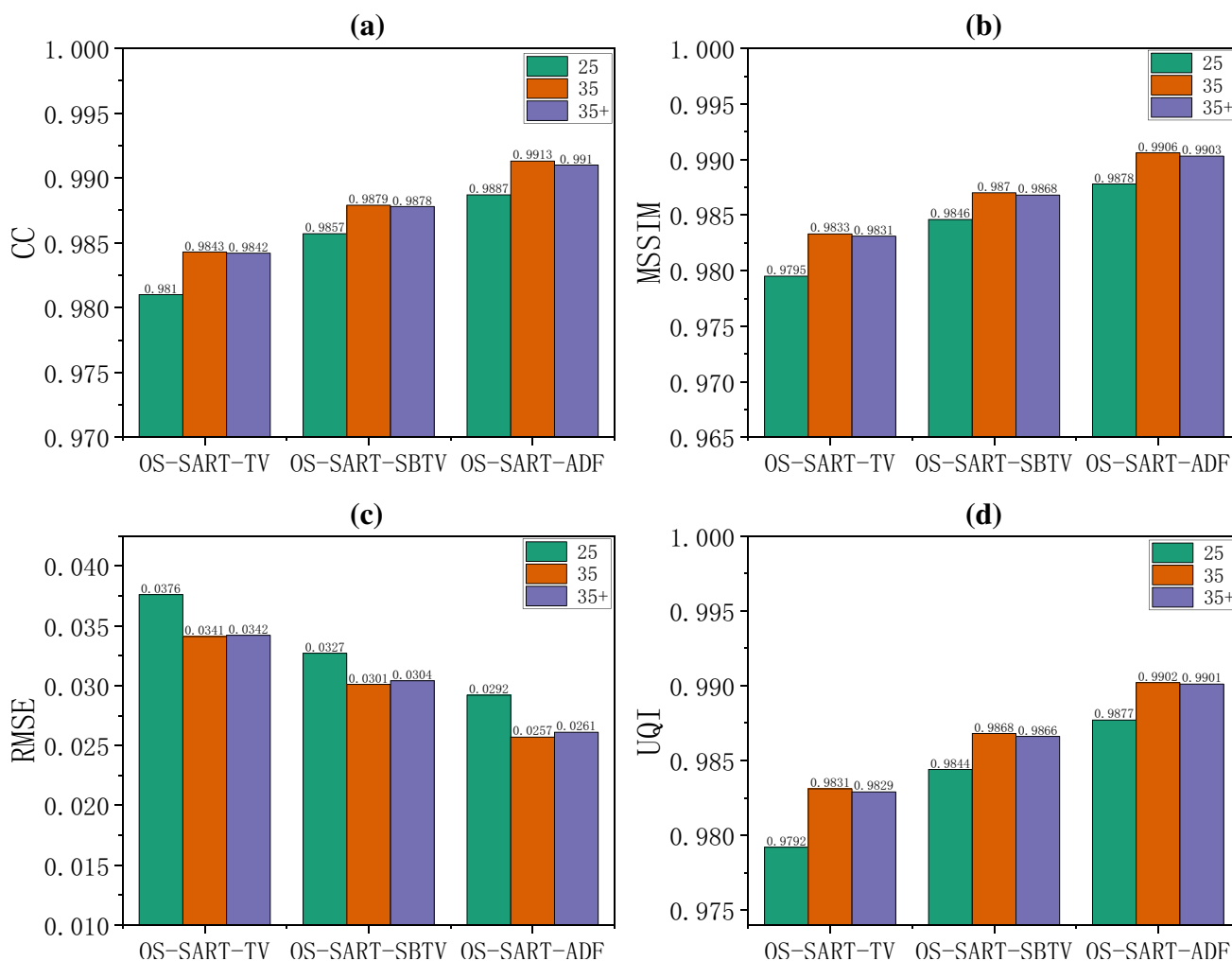
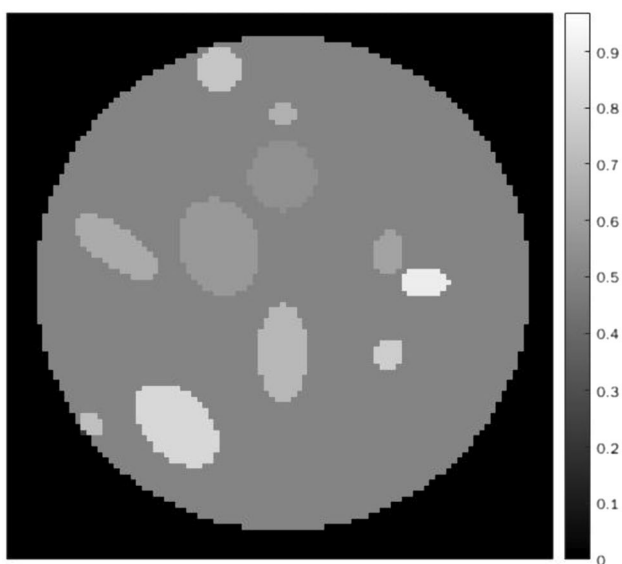**Fig. 5** (Color online) Metrics of 3D Shepp–Logan model reconstructed images

Fig. 6 The 3D industrial phantom slice image at z = 128

different projection angles. Depending on the reconstructed results of the algorithm, the larger the projection angle, the clearer the edge structure of the reconstructed image. In contrast to the other algorithms, the reconstructed image of the FBP algorithm is blurred, and the information of the image edge structure is significantly lost. By analyzing the reconstruction results of each algorithm, the OS-SART-TV algorithm reconstructed a more delicate image structure that was excessively smooth. Among these iterative algorithms, OS-SART-ADF reconstructs the image with the clearest edge structure and least noise effect.

As shown in Fig. 8, we performed a quantitative analysis of the rebuilt results using the three iterative algorithms. Initially, the reconstructed images for each algorithm were analyzed using noiseless projection data. Figure 8 shows that the CC, MSSIM, and UQI metrics of all the algorithms progressively increased as the projection angle increased. The three indicators exhibited similar trends. Based on the RMSE metric presented in
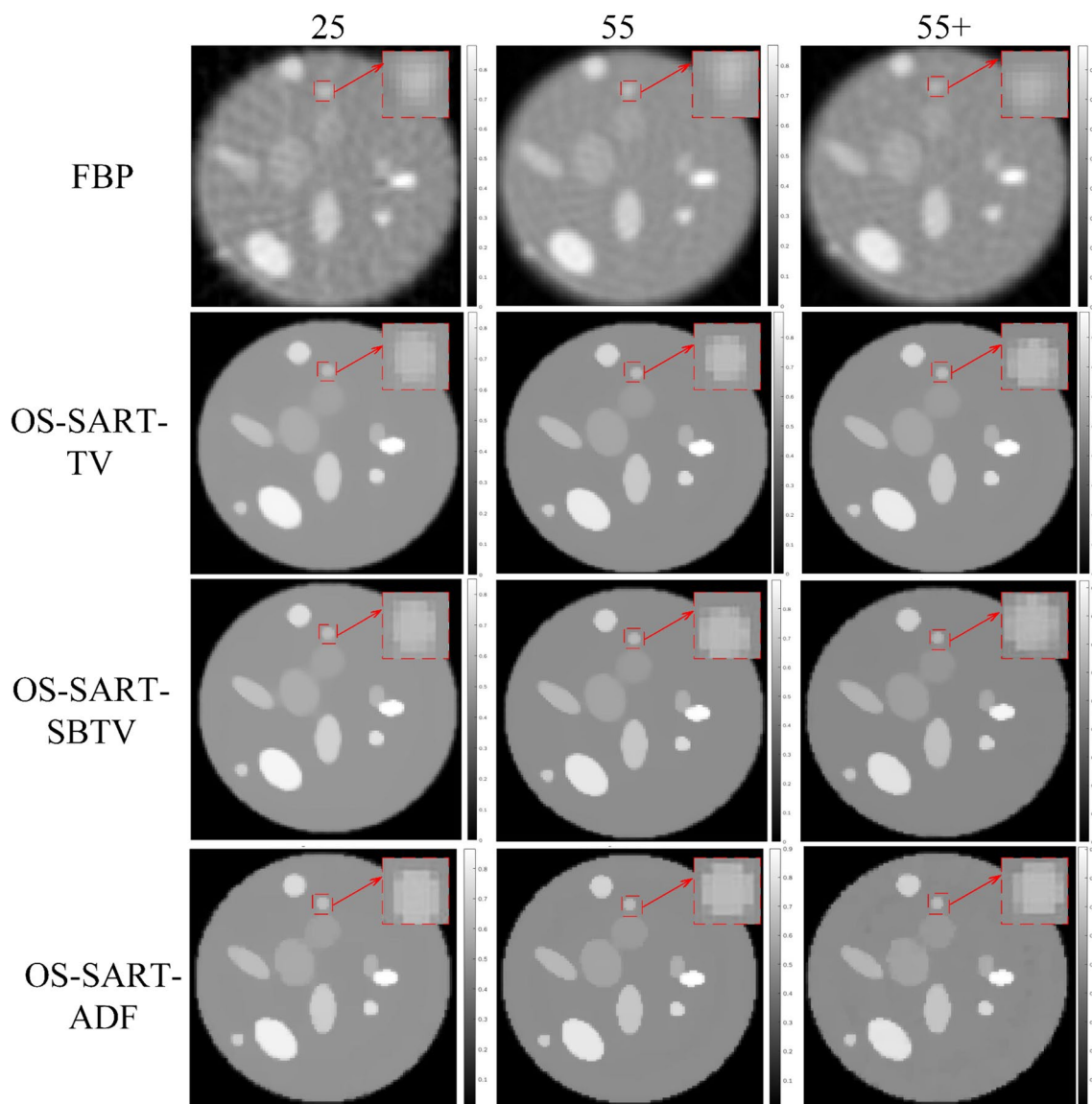
Fig. 7 Sliced images of the 3D industrial phantom at z = 128 for the four algorithms

Fig. 8, the OS-SART-ADF-reconstructed image had the lowest RMSE. For instance, when 25 projection views were reconstructed, the RMSE of OS-SART-ADF was 0.0079, indicating that the reconstructed image from this algorithm was the closest to the real image. As shown in Fig. 8d, the UQI of all algorithms progressively increases with an increase in the number of projected views, which is opposite to the trend of the RMSE. Among all reconstruction algorithms, the OS-SART-ADF-reconstructed images have the highest UQI, which indicates superior performance. For example, the UQI of OS-SART-ADF was 0.9978 when the number of reconstruction angles was 25. Subsequently, we performed a quantitative analysis of the reconstructed images containing noise. The CC, MSSIM, and UQI metrics in Fig. 8 show that the

OS-SART-ADF algorithm reconstructed images with the highest metrics when reconstructing the same amount of projection data containing noise. Furthermore, the RMSE metric in Fig. 8 indicates that the reconstructed images of the OS-SART-ADF algorithm had the smallest RMSE value. Thus, a quantitative and intuitive analysis of each algorithm indicates that OS-SART-ADF reconstructs the best images among all tested algorithms with the same number of reconstruction.

3.5 Real neutron projection experiment

We compared the reconstruction capabilities of all algorithms using a clock model (Fig. 9) with projection data provided by Schillinger [41]. Figure 10 shows a slice image
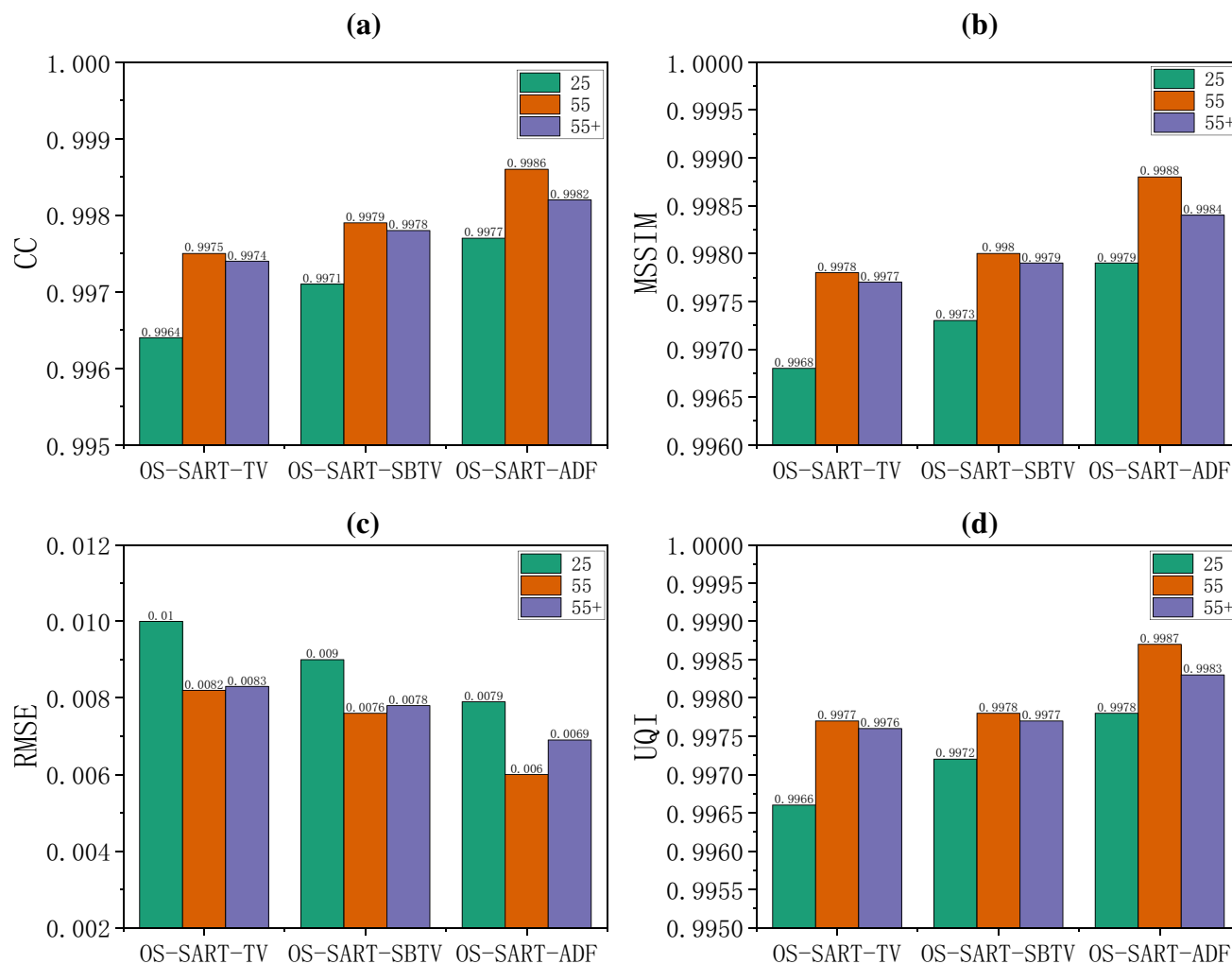
(a)

(b)

(c)

(d)

Fig. 8 (Color online) Evaluation metrics for the 3D industrial phantom reconstructed images

of the clock model at $z = 201$. The following three-step process was applied to the neutron photographs to obtain valid neutron projection data: First, for the dark- and bright-field images, white noise in the image was removed using a 5×5 median filter. For the neutron photographic image, 3×3 median filtering was applied, which not only protected the detailed information of the neutron photographic image, but also removed white noise from the image. Second, the pixel values of the dark-field and bright-field images provided are averaged separately, and the averaged dark-field background image data are subtracted from the averaged bright-field image data so that the corrected bright-field image data can be obtained. Finally, the entire neutron photographic image data were subtracted from the averaged dark-field image data, normalized, and negatively notated. The non-negative data were then corrected to obtain the neutron projection data for the applied image reconstruction.

As shown in Fig. 11, the image recreated using the FBP algorithm contained significant artifacts. The three iterative reconstruction algorithms eliminated artifacts better and reconstructed more image information than the FBP algorithm. Compared with the FBP algorithm, the reconstructed images from OS-SART-TV have fewer artifacts; however, because of the excessively smooth image edges of OS-SART-TV, a significant amount of the structural information of the images is lost. While the reconstructed image of OS-SART-SBTV is sharper than that of OS-SART-TV, it is still fuzzy compared to that from OS-SART-ADF. Therefore, OS-SART-ADF exhibits good performance in artifact suppression and noise reduction based on the visual observation of the reconstructed images.

As shown in Fig. 12, we quantitatively analyzed the clock model images reconstructed using the three iterative algorithms. From the RMSE metric shown in Fig. 12, it can be seen that OS-SART-ADF has the minimum RMSE,
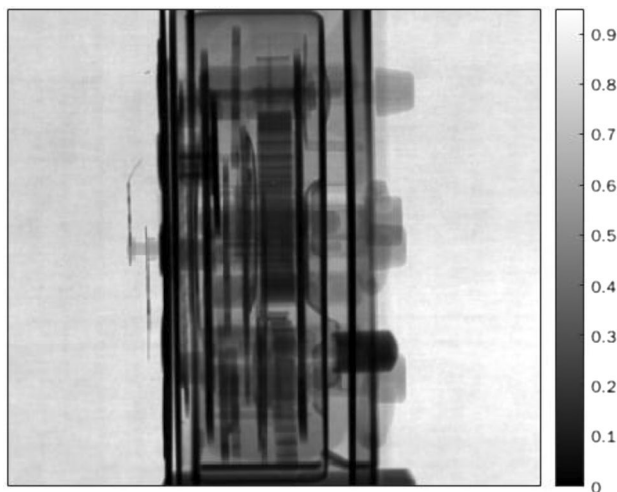
Fig. 9 (Color online) Clock model

Fig. 10 The clock model slices the image at z = 201

which means that the reconstructed image of OS-SART-ADF is the closest to the reference image. Moreover, the CC, MSSIM, and UQI of OS-SART-ADF were the largest among all algorithms. In conclusion, the OS-SART-ADF applied to neutron CT 3D reconstruction performed excellently in fine-structure reconstruction, noise removal, and

artifact suppression, which shows that the OS-SART-ADF algorithm is appropriate for neutron CT 3D reconstruction of sparse views.

4 Discussion

In this study, a high-performance sparse-view neutron CT 3D reconstruction algorithm was proposed. We used an iterative reconstruction algorithm in an NCT system to overcome the inherent shortcomings of the analytical algorithm (FBP), which prevents it from being applied to sparse-view reconstruction. Regular terms are introduced into the iterative algorithm to adjust the reconstructed image and make it more effective for use in NCT systems. Owing to the photon statistical noise and electronic device noise, the neutron projection data acquired by the NCT system contained a large amount of noise, resulting in poor-quality reconstructed images. As a result, to enhance the imaging performance of NCT systems, it is necessary to enhance the processing of neutron images. This requires the algorithms used in NCT systems not only to remove noise efficiently, but also to retain more information about the image edge structure. The PDE-based anisotropic diffusion model can reduce noise by enhancing the diffusion of the flat areas of the image. At the same time, this model can also be used to reduce the diffusion of image edges and preserve edge detail information. This is because the PDE-based image-processing method only smooths the parallel edges of the projected data and not the vertical edges, thus preserving the main features of the image while reducing noise and smoothing the image. The anisotropic diffusion filtering algorithm can effectively suppress the noise in the projection data and preserve the image edge structure information by reducing the diffusion of the image edges. The algorithm presented in this study performed well for the reconstruction of NCT projection data as confirmed from the results of the reconstructed images. Compared with FBP, the TV-based regularization algorithm can remove image noise to some extent; however, the reconstructed image is so smooth that some information about the image appears to be lost. This is because denoising an image using the variational method produces an intermediate value, which may result in an overly smooth image. Therefore, we present OS-SART-ADF, which is based on an anisotropic diffusion model. The reconstructed results of the 3D Shepp–Logan model, 3D industrial, and clock models demonstrate the exceptional performance of OS-SART-ADF in both quantitative and visual analyses. For example, the RMSE of the OS-SART-ADF-reconstructed image when reconstructing a 3D Shepp–Logan model with 25 projection views is 0.0292. The reconstructed image also had the highest UQI, MSSIM, and CC among all the
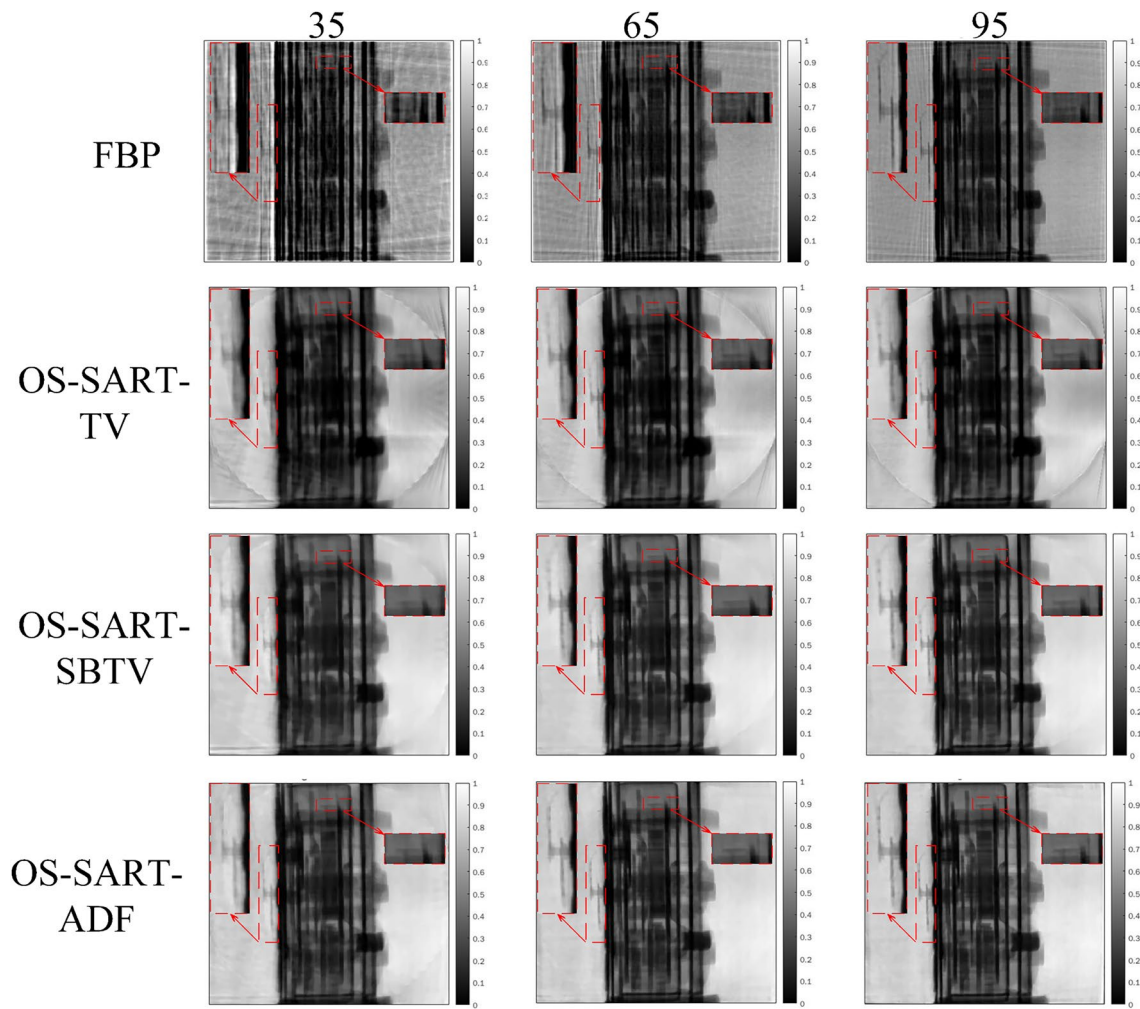
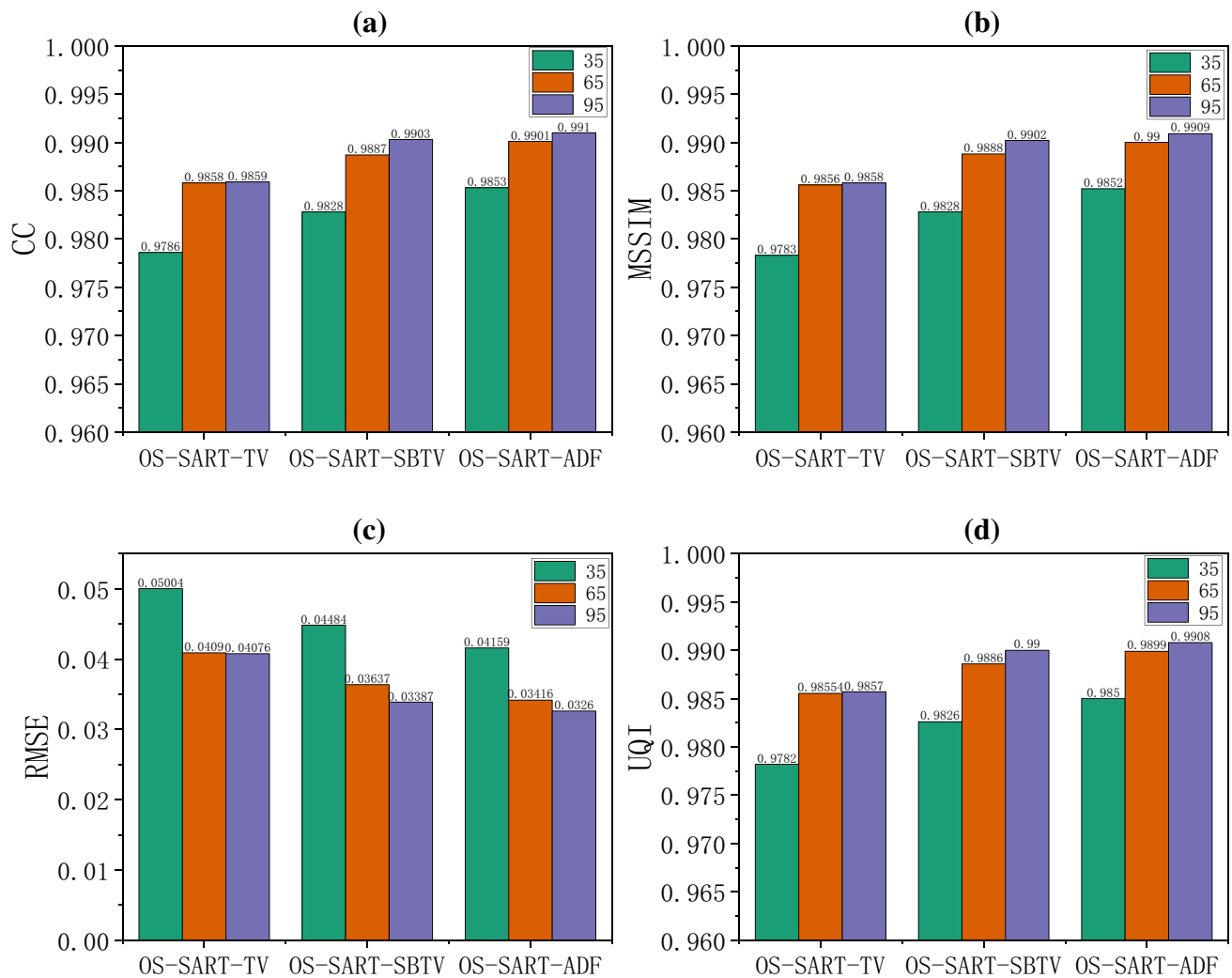**Fig. 11** Slice image of the reconstructed image of the four algorithms at $z = 201$

Fig. 12 Metrics for quantitative analysis of reconstructed clock model images

algorithms, measuring 0.9877, 0.9878, and 0.9887, respectively. This illustrates that OS-SART-ADF produced the best reconstructed images.

5 Conclusion

NCT is a nondestructive testing technique that can quickly and accurately detect the internal structure of a sample, and is extensively used in nuclear engineering, aerospace technology, and military applications. Owing to the long scanning time and complex application environment of NCT, the quality of the obtained neutron projection data is relatively poor. Therefore, an NCT system must use efficient image reconstruction algorithms to reconstruct high-quality images. To meet this requirement, we propose the OS-SART-ADF algorithm to be used for NCT-sparse

reconstruction. The OS-SART-ADF algorithm comprises two processes: OS-SART is used to reconstruct the image, and ADF is used for image filtering, denoising, and preserving the image edge structure information. As confirmed from quantitative and visual analyses of digital 3D Shepp–Logan, 3D industrial phantom, and clock model reconstructed images, OS-SART-PDTV exhibited superior performance in suppressing artifacts, reconstructing fine structures, and removing noise compared to other algorithms. From the RMSE metric in Fig. 5, it was seen that the OS-SART-ADF-reconstructed images had the minimum RMSE values under the same conditions.

versions of the manuscript. All authors read and approved the final manuscript.

Data availability The data that support the findings of this study are openly available in Science Data Bank at https://doi.org/https://doi.org/10.57760/sciencedb.j00186.00387 and https://cstr.cn/31253.11.sciencedb.j00186.00387.

Declarations

Conflict of interest The authors declare that they have no competing interests.

References

1. U. Garbe, T. Randall, C. Hughes et al., A new neutron radiography/tomography/imag-ing station DINGO at OPAL. Phys. Procedia **69**, 27–32 (2015). https://doi.org/10.1016/j.phpro.2015.07.003

2. W.T. Hsiao, W.C. Kuo, H.H. Lin, L.H. Lai, Assessment and feasibility study of lemon ripening using X-ray image of information visualization. Appl. Sci. **11**, 3261 (2021). https://doi.org/10.3390/app11073261

3. D. Schwarz, P. Vontobe, E.H. Lehmann et al., Neutron tomography of internal structures of vertebrate remains: a comparison with X-Ray computed tomography. Palaeontol. Electron. **8**(2), 30A (2005)

4. M. Zanarini, P. Chirco, M. Rossi et al., Evaluation of hydrogen content in metallic samples by neutron computed tomography. IEEE Trans. Nucl. Sci. **42**, 580 (1995). https://doi.org/10.1109/23.467910

5. H. Isaksson, S. Le Cann, C. Perdikouri et al., Neutron tomographic imaging of bone-implant interface: comparison with X-ray tomography. Bone **103**, 295 (2017). https://doi.org/10.1016/j.bone.2017.07.022

6. S. Le Cann, E. Tudisco, C. Perdikouri et al., Characterization of the bone-metal implant interface by Digital Volume Correlation of in-situ loading using neutron tomography. J. Mech. Behav. Biomed. Mater. **75**, 271 (2017). https://doi.org/10.1016/j.jmbbm.2017.07.001

7. C. Zanolli, B. Schillinger, A. Beaudet et al., Exploring hominin and non-hominin primate dental fossil remains with neutron microtomography. Phys. Procedia **88**, 109 (2017). https://doi.org/10.1016/j.phpro.2017.06.014

8. N. Kardjilov, A. Hilger, I. Manke et al., Neutron tomography in archaeology. Mater. TEST **57**, 324 (2015). https://doi.org/10.3139/120.110708

9. N. Kardjilov, G. Festa (eds.), *Neutron methods for archaeology and cultural heritage* (Springer, Switzerland, 2017)

10. H.Y. Lan, T. Song, Z.H. Luo et al., Isotope-sensitive imaging of special nuclear materials using computer tomography based on scattering nuclear resonance fluorescence. Phys. Rev. Applied **16**, 054048 (2021). https://doi.org/10.1103/PhysRevApplied.16.054048

11. X.F. Jiang, J.R. Zhou, H. Luo et al., A large area 3He tube array detector with vacu-um operation capacity for the SANS instrument at the CSNS. Nucl. Sci. Tech. **33**, 89 (2022). https://doi.org/10.1007/s41365-022-01067-1

12 M. Kureta, H. Iikura, Development of an ultra-high-speed scanning neutron tomography system for high-quality and four-dimensional visualizations. Nucl. Instrum. Methods Phys. Res. Sect. A **605**, 81 (2009). https://doi.org/10.1016/j.nima.2009.01.164

13. S. Li, Z. Dong, Q. Gan et al., A MLEM-TV-MRP algorithm for fast neutron computed tomography reconstruction of high statistical noise and sparse sampling. IEEE Access **8**, 3397 (2019). https://doi.org/10.1109/ACCESS.2019.2959340

14. W.B. He, Y.G. Ma, L.G. Pang et al., High-energy nuclear physics meets machine learning. Nucl. Sci. Tech. **34**, 88 (2023). https://doi.org/10.1007/s41365-023-01233-z

15. Y. Kiyanagi, Neutron applications developing at compact accelerator-driven neutron sources. AAPPS Bull. **31**, 22 (2021). https://doi.org/10.1007/s43673-021-00022-3

16. H. Hotchi, High-power proton accelerators for pulsed spallation neutron sources. AAPPS Bull. **31**, 23 (2021). https://doi.org/10.1007/s43673-021-00025-0

17. Y. Bae, D.S. Kim, H.J. Seo et al., Advances of LINAC-based boron neutron capture therapy in Korea. AAPPS Bull. **32**, 34 (2022). https://doi.org/10.1007/s43673-022-00063-2

18. B. Hong, Status of the RAON project in Korea. AAPPS Bull. **33**, 3 (2023). https://doi.org/10.1007/s43673-022-00074-z

19. L.X. Zhang, S.Z. Chen, Z.D. Zhang et al., Resolution analysis of thermal neutron rad-iography based on accelerator-driven compact neutron source. Nucl. Sci. Tech. **34**, 76 (2023). https://doi.org/10.1007/s41365-023-01227-x

20. A.H. Andersen, Algebraic reconstruction in CT from limited views. IEEE Trans. Med. Imaging **8**, 50 (1989). https://doi.org/10.1109/42.20361

21. R. Gordon, R. Bender, G.T. Herman, Algebraic Reconstruction Techniques (ART) for three-dimensional electron microscopy and X-ray photography. J. Theor. Biol. **29**, 471 (1970). https://doi.org/10.1016/0022-5193(70)90109-8

22. P. Gilbert, Iterative methods for the three-dimensional reconstruction of an object from projections. J. Theor. Biol. **36**, 105 (1972). https://doi.org/10.1016/0022-5193(72)90180-4

23. A.H. Andersen, A.C. Kak, Simultaneous Algebraic Reconstruction Technique (SART): A superior implementation of the ART algorithm. Ultrason. Imaging **6**, 81 (1984). https://doi.org/10.1016/0161-7346(84)90008-7

24. L.I. Rudin, S. Osher, E. Fatemi, Nonlinear total variation based noise removal algorithms. Phys. D **60**(1–4), 259–268 (1992). https://doi.org/10.1016/0167-2789(92)90242-F

25. H. Li, X. Chen, Y. Wang et al., Sparse CT reconstruction based on multi-direction anisotropic total variation. Biomed. Eng. Online **13**, 92 (2014). https://doi.org/10.1186/1475-925X-13-92

26. Z. Chen, X. Jin, L. Li, A limited-angle CT reconstruction method based on anisotropic TV minimization. Phys. Med. Biol. **58**, 2119 (2013). https://doi.org/10.1088/0031-9155/58/7/2119

27. Z. Tian, X. Jia, K. Yuan et al., Low-dose CT reconstruction via edge-preserving total variation regularization. Phys. Med. Biol. **56**, 5949 (2011). https://doi.org/10.1088/0031-9155/56/18/011

28. H. Qi, Z. Chen, L. Zhou, CT image Rreconstruction from sparse projections using adaptive TpV regularization. Comput. Math. Method M. **2015**, 354869 (2015). https://doi.org/10.1155/2015/354869

29. P. Perona, J. Malik, Scale-space and edge detection using anisotropic diffusion. IEEE Trans. Pattern Anal. Mach. Intell. **12**(7), 629–639 (1990). https://doi.org/10.1109/34.56205

30. Y.L. You, M. Kaveh, Fourth-order partial differential equations for noise removal. IEEE Trans. Image Process. **9**(10), 1723–1729 (2000). https://doi.org/10.1109/83.869184

31. J. Bai, X.C. Feng, Fractional-order anisotropic diffusion for image denoising. IEEE Trans. Image Process. **16**(10), 2492–2502 (2007). https://doi.org/10.1109/TIP.2007.904971

32. F. Catté, P.L. Lions, J.M. Morel et al., Image selective smoothing and edge detecti-on by nonlinear diffusion. SIAM J. Numer. Anal. **29**(1), 182–193 (1992). https://doi.org/10.1137/0729012

33. L.M. Bregman, The relaxation method of finding the common point of convex sets and its application to the solution of problems in convex programming. USSR Comput. Appl. Math **7**(3), 200–217 (1967). https://doi.org/10.1016/0041-553(67)90040-7

34. J. Sheng, B. Chen, Y. Ma et al., A novel reconstruction approach combining OSEM and split Bregman method for low dose CT. Biomed. Signal Process. Control **62**, 102095 (2020). https://doi.org/10.1016/j.bspc.2020.102095

35. T. Goldstein, S. Osher, The split Bregman method for L1-regularized problems. SIAM J. Imaging Sci. **2**(2), 323–343 (2009). https://doi.org/10.1137/080725891

36 X.C. Tai, K. Mørken, M. Lysaker et al. (eds.), *Scale space and variational methods in computer vision: second international conference* (Springer, Berlin, Heidelberg, 2009)

37. J. Tang, Q. Sun, A 3-D anisotropic diffusion filter for speckle reduction in 3-D ultrasound images. SPIE. **7239**, 267–275 (2009). https://doi.org/10.1117/12.808462

38. D. Zeng, J. Huang, Z. Bian et al., A simple low-dose x-ray CT simulation from high dose scan. IEEE Trans. Nucl. Sci. **62**(5), 2226–2233 (2015)

39. G.F. Long, G.R. Feng, P. Sprenger, Overcoming synthesizer phase noise in quantum sensing. Quantum Eng. **1**(4), e27 (2019). https://doi.org/10.1002/que2.27

40. H. Jiang (ed.), *Computed tomography: principles, design, artifacts, and recent advances* (SPIE, Bellingham, Washington, 2009)

41. B. Schillinger, A.E. Craft, A freeware path to neutron computed tomography. Phys. Procedia **88**, 348 (2017). https://doi.org/10.1016/j.phpro.2017.06.047

Authors and Affiliations

Yang Liu[1,2] · **Teng-Fei Zhu[1]** · **Zhi Luo[1]** · **Xiao-Ping Ouyang[1,3]**

✉ Yang Liu
yliu@ncepu.edu.cn

1 School of Nuclear Science and Engineering, North China Electric Power University, Beijing 102206, China

2 State Key Laboratory of Nuclear Resources and Environment, East China University of Technology, Nanchang 330013, China

3 State Key Laboratory of Intense Pulsed Radiation Simulation and Effect, Xi'an 710024, China